CHEMISTRY OF MATERIALS

pubs.acs.org/cm

Article

Unraveling Thermally Regulated Gating Mechanisms in TPT Pore-Partitioned MOF-74: A Computational Endeavor

Gavin A. McCarver,* Morgan J. Kramer, Taner Yildirim, and Wei Zhou

Cite This: *Chem. Mater.* 2024, 36, 8098−8106

Read Online

ACCESS | Metrics & More | Article Recommendations | Supporting Information

ABSTRACT: In the pursuit of advanced gas adsorption materials, we investigate the thermally activated gating mechanism of functionalized TPT (2,4,6-tri(4-pyridyl)-1,3,5-triazine) ligands within the one-dimensional channels of Mg-MOF-74. These ligands induce the formation of ultramicroporous windows, whose sizes dynamically respond to substituent groups and temperature. Gas-phase DFT calculations reveal molecular rotator behavior in the TPT-X (X = H, F, CH_3, Cl) ligands showing an inverse steric relationship between the functional group size and the barrier for rotation, indicating a propensity for larger functional groups to facilitate molecular rotation. Once incorporated into the channel of MOF-74, the larger functional groups result in energy landscapes marked by higher barriers, suggesting that portions of the landscape are only accessible at higher temperatures. These findings suggest temperature-driven pore size changes, hinting at thermally regulated gating. Molecular dynamics (MD) calculations corroborate these findings, showing an increase in the pore size of the −Cl and $-CH_3$ functionalized systems with increasing temperature. Comparative analysis highlights TPT-X pore partitioned MOF-74's (mTPT-X) superiority over other ultramicroporous MOFs, making them promising for gas adsorption and separation applications. At lower (10% maximum) loading, the materials demonstrate ultramicroporosity with pore volumes akin to MOF-74, potentially leading to temperature-driven high capacity gas storage and gas separation. Conversely, higher loading (50% maximum) leads to a loss of pore volume and a subsequent loss of capacity, leading to lower feasibility for gas storage but potentially enhancing gas separation processes.

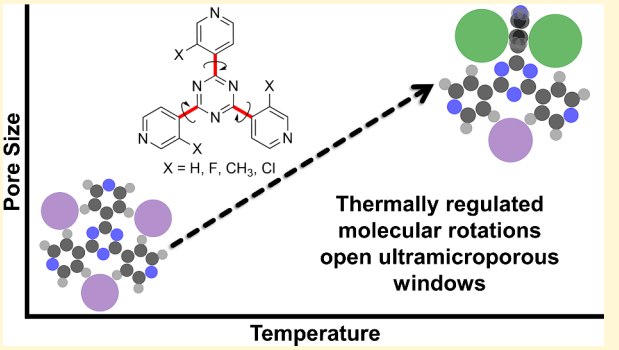

INTRODUCTION

Porous materials are highly valued for their exceptional properties in gas adsorption, separation, and storage applications. Metal−organic frameworks (MOFs) stand out as an exceptionally versatile class of porous materials.[1,2] MOFs offer a remarkable degree of tunability, allowing precise control over properties such as surface area, pore volume, and pore window size. This tunability stems from the vast array of possible combinations of organic linkers and metal ions or clusters, leading to the creation of thousands of unique MOFs.[3−5]

In recent years, a subclass of MOFs with pores less than 5 Å (known as ultramicroporous MOFs),[5−8] has garnered significant attention for their outstanding capabilities for gas adsorption. The ultramicroporosity observed in these MOFs often arises from specific design strategies. For instance, ultramicroporosity can be achieved by employing extremely small organic linkers like formate in ALF (aluminum formate)[9] or cyanide in Prussian Blue analogues during synthesis.[10] Alternatively, ultramicroporosity may result from MOF topologies characterized by exceptionally small pore windows, as seen in structures like Cu-ATC[11] (ATC: 1,3,5,7-adamantane tetracarboxylate) or MUV-26 (MUV: Materials of the University of Valencia).[12]

Another effective strategy for designing ultramicroporous MOFs is through pore-space partitioning (PSP).[13] This approach can allow for a significant reduction in the pore window size of a MOF while preserving the pore volume. By narrowing the pore windows, PSP effectively creates ultramicroporosity, leading to improved gas adsorption and storage capabilities. The PSP approach has been shown to yield MOFs with enhanced properties, such as increased CO_2 and improved H_2 uptake.[14,15]

One PSP technique involves the introduction of an organic ligand into the MOF's pore either during the synthesis process as a template strategy or through a postsynthetic modification step. The selection of the organic ligand is often tailored to the

Received: June 18, 2024
Revised: July 24, 2024
Accepted: July 25, 2024
Published: August 8, 2024

Downloaded via NATL INST OF STANDARDS & TECHNOLOGY on October 25, 2024 at 19:23:54 (UTC).
See https://pubs.acs.org/sharingguidelines for options on how to legitimately share published articles.

ACS Publications

© 2024 American Chemical Society

specific MOF, with di-, tri-, and hexatopic ligands being commonly employed.[16] One recurring ligand utilized in PSP is 2,4,6-tri(4-pyridyl)-1,3,5-triazine (TPT). The size and symmetry of TPT closely match the pore size of several MOFs, including Mg-MOF-74[17,18] (see Figure 1A) and MIL-88.[15,19−22]

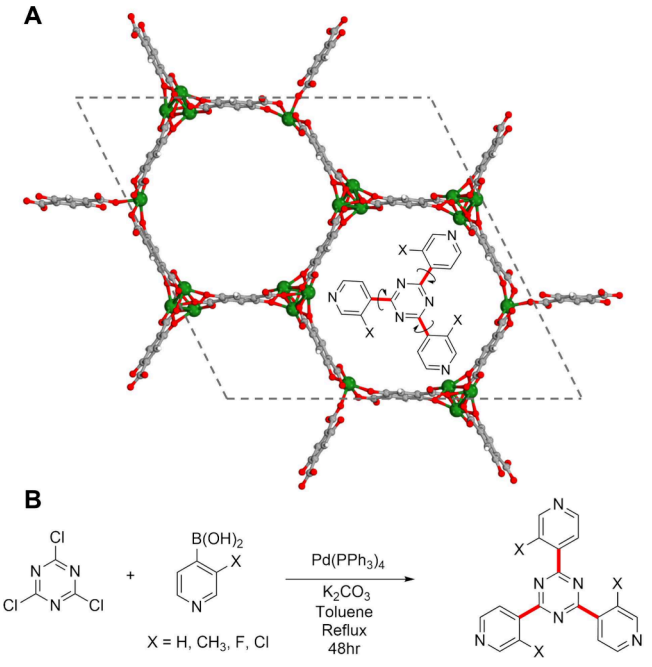

Figure 1. A - Atomic model of the MOF-74 unit cell with an incorporated TPT-X ligand, illustrating rotation about the T4P bond. Color code: H (white), C (gray), O (red), Mg (dark green). **B** - Potential synthetic pathway for synthesizing TPT-X type ligand scaffolds via Suzuki coupling. The bold, red bond indicates the T4P bond.

In this work, we aimed to examine the differences that arise from the pore-space partitioning of the 1-dimensional channels of Mg-MOF-74 (simply referred here as MOF-74) with functionalized TPT ligands. Based on synthetic literature, we suspect that a series of TPT-X (X = H, CH_3, F, Cl) ligands can be readily synthesized. Suzuki coupling procedures utilizing cyanuric chloride as a coupling partner to boronic acids has been described previously and could yield the 3-X pyridyl substituted analogues of TPT. One suggested pathway is shown in Figure 1B. The synthesis of 1,3,5 triaryl triazines has been achieved via numerous synthetic pathways, including cylcization reactions of the nitriles catalyzed by SmI_2 catalyst,[23] as well as the co-condensation of aryl aldehydes and aryl amidines.[24,25] While the synthesis of TPT-X ligands has not been conducted as part of this computational study, the proposed synthetic route highlights the potential feasibility of future experimental work. Our computational findings aim to provide a theoretical foundation for the subsequent synthesis and practical application of TPT-X loaded MOF-74 materials.

These TPT-X ligands are expected to introduce significant changes compared to the TPT (herein referred to as TPT-H) ligand itself. One of the most immediate effects is a reduction in the pore window size, attributed to the larger functional groups replacing hydrogen atoms. Furthermore, the introduction of these functional groups results in an additional property that is not immediately apparent: a modulation in the barrier toward rotation about the triazine-4-pyridyl (T4P) bond (see red bonds in Figure 1A,B). This rotational motion effectively allows the TPT-X ligands to act as molecular rotators.[26,27] Prior investigations have examined this behavior in the organic framework that MOFs are composed of,[28−33] but we have not identified similar investigations related to pore-partitioning agents in MOFs. A consequence of these reduced rotational barriers is the emergence of a temperature-dependent pore window size, approximated as the pore limiting diameter (PLD), which expands with increasing temperatures. This phenomenon hints at the presence of a potential thermally regulated gating mechanism within the framework of MOF-74, akin to the processes observed in flexible MOFs that can dynamically open and close their pore apertures.[34,35]

This work is structured to provide a comprehensive theoretical analysis of the effects of functionalized TPT-X ligands on the properties of MOF-74. We start by presenting a comparative study among the four TPT-X ligands in the gas-phase, focusing on their role as molecular rotators. This analysis involves examining the potential energy surface of the dihedral angle formed across the T4P bond, shedding light on the rotational dynamics of the ligands. Next, we investigate how the molecular rotator behavior of the TPT-X ligands changes upon incorporation into the channels of MOF-74. This is followed by an examination of the impact of TPT-X ligands on the pore structure of MOF-74, specifically looking at changes in surface area, pore volume, and pore window size. We then explore the temperature-dependent gating mechanism observed in MOF-74 with TPT-X ligands, facilitated by the molecular rotators, highlighting variations in pore window size with changing temperatures. Finally, we discuss the implications of our theoretical findings and their potential applications in gas storage, separation, and related fields.

COMPUTATIONAL METHODS

Gas-Phase Density Functional Theory (DFT) Calculations. To examine the gas-phase behaviors of the TPT ligands, we employ gas-phase DFT calculations with the r^{2}SCAN-3c composite method[36,37] as it has been shown to be a robust method for thermochemistry, geometries, and noncovalent interactions. Other common density functionals resulted in very similar behaviors (Figure S1). The r^{2}SCAN-3c composite method assigns the def2-mTZVPP basis set[38] to each atom combined with D4 dispersion corrections[39] and the geometrical counter-poise correction.[40] We utilize the resolution of identity (RI) method to accelerate the computation of the four-index integrals and assign each atom the def2/J auxiliary basis set.[41]

To construct the energy diagram for the molecular rotator, we scan the dihedral angle between the 3 and 5 positions of the pyridine moiety and the 2 and 4 positions of the triazine moiety. This scan is performed between 0° and 359°. Frequency calculations are performed analytically using the quasi-rigid rotor harmonic oscillator (Qausi-RRHO) approximation assuming a temperature of 298.15K. Standard SCF and optimization criteria are used. These calculations are conducted using the ORCA 5.0 software package.[42]

Semiempirical Tight Binding Calculations. Semiempirical tight binding calculations were performed using the XTB program by Grimme et al.[43] Standard optimization and SCF criteria were applied except for the Broyden damping value was changed from 0.4 to 0.2 for SCF convergence. A segment of MOF-74 approximately 40 Å in length (Figure S1) was used for these calculations, with dangling valencies on the ligands capped. During the optimization steps, the atoms of the MOF section were assumed to be frozen.

Multiscale Calculations. Multiscale calculations were performed using a dual-level approach, incorporating the aforementioned DFT protocol as the higher level and XTB as the lower level. In these

https://doi.org/10.1021/acs.chemmater.4c01699
Chem. Mater. 2024, 36, 8098−8106

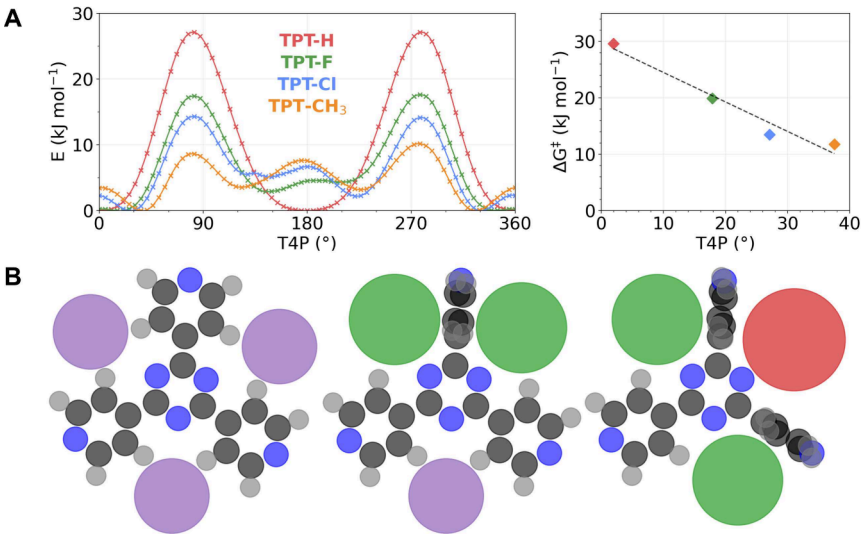

Figure 2. A - Left: Potential energy profile along the T4P bond of the TPT-X ligands. Data points obtained from *ab initio* calculations are represented by crosses (x) and smoothed using a cubic spline function. Right: Equilibrium T4P angle plotted against the free energy barriers of rotation ($\Delta G^{\ddagger}$) for each TPT-X ligand. The linear regression line is shown as a dashed line. Color code: TPT-H (red), TPT-F (green), TPT-CH_3 (blue), TPT-Cl (yellow). **B** - Largest spheres capable of fitting between the TPT-H ligand and the walls of MOF-74 following rotation of zero (left), one (middle), and two (right) T4P bonds. Purple spheres represent a size of 2.43 Å, green spheres represent a size of 3.10 Å, and red spheres represent a size of 3.19 Å. Color code: light gray (H), dark gray (C), blue (N).

calculations, a small segment of the one-dimensional channel of MOF-74 (~12 Å, Figure S3) was constructed, with dangling valencies on the ligands capped. During optimizations, the MOF atoms (analyzed at the lower level of theory) were constrained to their initial positions, while only the TPT-X ligands (analyzed at the higher level of theory) were allowed to relax.

Molecular Dynamics (MD) Calculations. We employ LAMMPS[44] for conducting MD simulations. Each simulation consists of a 1 ns NVE (constant number of particles, volume, and energy) equilibration run followed by a 10 ns NVT (constant number of particles, volume, and temperature) run, where a Langevin thermostat is utilized. The UFF4MOF force field[45] is employed, and LAMMPS input files are generated using the lammps-interface Python code.[46] Atomic charges are assigned using a message-passing neural network (MPNN).[47] Cartesian coordinates are recorded every 5 ps, resulting in a total of 2001 sets of coordinates for each temperature-material combination. To ensure each simulation does not undergo substantial translation motion, we apply a harmonic potential equal to 50 kcal mol^{-1} relative to the original atomic positions. The structures are composed of a 1 × 1 × 5 supercell of MOF-74 with either one or five TPT-X ligand in each one-dimensional channel. This is equivalent to a 10% and 50% loading in the material. Subsequently, the PoreBlazer program[48] is applied to analyze the pore size distribution (PSD) for each set of Cartesian coordinates. This PSD data is then averaged across the entire 2001 sets of coordinates obtained during the 10 ns NVT run. We found that a 10 ns production run was sufficient to reach equilibrium for several properties including energy and temperature (see Figures S4−S8). From this data, pore limiting diameters (PLD), largest cavity diameters (LCD), accessible surface areas (ASA), and helium pore volumes (HePV) are extracted to facilitate comparison among different mTPT-X materials. Additionally, we perform simulated annealing simulations by constantly lowering the temperature of an NVE simulation from 400 K to 0K over a time range of 1 ns.

RESULTS

Rotational Dynamics of the TPT-X Ligands. The rotation about the T4P bond allows us to closely examine how the molecular rotator behavior changes with the functionalization of the TPT-X ligands, furthering our understanding of the thermal gating mechanism in pore-partitioned MOF-74 materials. These calculations are conducted in the gas-phase (see methods section for details) by incrementally adjusting the dihedral angle formed across a T4P bond. This incremental movement enables us to observe how the energy of rotation changes from the scenario where the X-groups are furthest away and in different void spaces (as illustrated in Figure 1) to when they are closest and occupy the same void space.

The left side of Figure 2A illustrates the one-dimensional energy landscape for the rotation about the T4P bond in each TPT-X ligand. The replacement of the H functional group at the 3-position of the pyridyl moiety breaks the symmetry of the T4P bond rotation, leading to a significant reduction in barrier height toward rotation. Other 3-fold symmetric molecules show a preference for propeller-like conformations, likely due to steric strain,[49−52] while the TPT-H ligand adopts a more planar conformation (equilibrium T4P dihedral angle of 2.0°) as the pyridyl rings are further apart. However, in their lowest energy conformations, the larger -F, $-CH_3$, and -Cl functional groups induce a loss of planarity and prefer a more propeller-like conformation, with T4P angles of 17.9°, 27.1°, and 37.5°, respectively. Molecular mechanics (MM) calculations using UFF at the DFT geometries yield similar energy landscapes, helping to justify the MD calculations discussed below using the TPT-X systems (top of Figure S9).

Plotting the activation energy ($\Delta G^{\ddagger}$) required for rotation about the T4P bond against the equilibrium T4P dihedral angle reveals a nearly linear trend (see right side of Figure 2A). This trend suggests that TPT-X ligands with larger equilibrium T4P dihedral angles result in lower rotational barriers. While inverse steric dependency has been observed previously for several molecular complexes including metal thiolate complexes, attributed to steric, enthalpic, and entropic contributions,[53,54] no similar study on TPT or similar ligands has been identified. By performing frequency calculations at the global maxima near 81° and minima of each respective potential energy surface, we found that both zero-point and enthalpic

https://doi.org/10.1021/acs.chemmater.4c01699
Chem. Mater. 2024, 36, 8098−8106

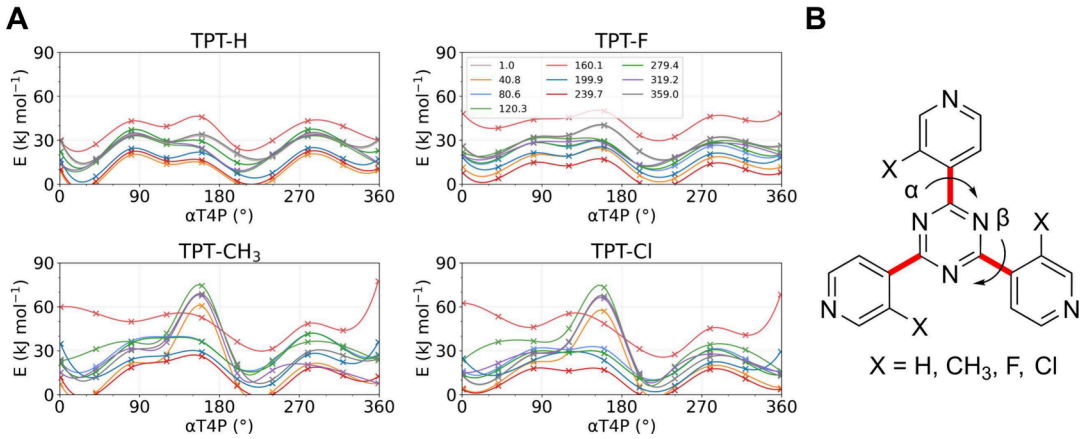

Figure 3. Potential energy profiles along two T4P bonds (α and β) of the TPT-X ligands. Data points obtained from the multiscale *ab initio* calculations are represented by crosses (x) and smoothed using a cubic spline function. Different colored lines correspond to different β angle values between 0° and 359° in increments of ~40°.

contributions lower the rotational barrier, while entropic contributions raise it (see Figure S10). Thus, the change in rotational barrier is a function of not only the size of the functional group at the 2-position of the pyridyl moiety but also the enthalpic and entropic contributions to the total energy of the system.

Utilizing this trend, we predict the rotational barrier for TPT-Br based on its optimized T4P dihedral angle of 39.4° to be slightly lower than TPT-Cl at 9.1 kJ mol^{-1}. However, the limited availability of the (3-bromopyridin-4-yl)boronic acid starting material and the difficulty of such a synthesis compared to fluoro- or chloro-functionalized boronic acids would limit its viability. The linear trend also allows us to predict that a TPT-X ligand with an equilibrium T4P angle of 56.9° would result in near barrier-less rotational motion, but identifying and synthesizing such a ligand may prove difficult due to secondary effects such as bond rotations present in larger functional groups such as -OCH_3 or −CH_2CH_3.

The energy landscapes also reveal a marked change in the region between dihedral angles of 120° and 240°. While this area exhibits a global minimum value for the TPT-H ligand due to symmetry, it displays both local maxima and minima for the other ligands. The presence of lower maxima and higher minima in this region indicates that the rotation about the T4P for the TPT-F, TPT-CH_3, and TPT-Cl ligands should be fairly facile. Beyond the temperatures at which this region may be accessed (the activation temperatures), these ligands could overcome the initial barrier from the equilibrium dihedral value to reside in this shallower region of the energy landscape. Consequently, the TPT-F, TPT-CH_3, and TPT-Cl ligands are expected to exhibit superior molecular rotator behavior in the gas-phase compared to TPT-H. By examining the energy landscape of two rotating T4P bonds, further evidence of the facile molecular rotator behavior of the TPT-F, TPT-CH_3, and TPT-Cl ligands is found (Figure S11). The energy landscapes for these ligands is quite flat compared to the TPT-H ligand, suggesting that in the gas-phase, they can readily rotate about any number of the T4P bonds.

By using a simplified model in which the TPT-H ligand is found within a circle the same size as the one-dimensional channel of MOF-74 (7.68 Å), we can approximate how much more space is made available following T4P bond rotation. Note that this model does not involve additional DFT calculations and instead uses the gas-phase optimized geometries discussed above. The largest sphere that can be accommodated between two adjacent tripyridyl moieties is assumed to be the point that maximizes the distance between the two moieties and the "wall" which is assumed to be a perfect circle. The TPT-H ligand can accommodate spheres of radii 2.43 Å at equilibrium (circles in Figure 2B and dark areas on the left-hand side of Figure S12). At the highest energy point where the T4P angle is 81°, the TPT-H ligand can now accommodate spheres of two sizes: 2.43 and 3.10 Å (purple and green circles in Figure 2B, respectively). The former sphere corresponds to the void space furthest from the rotator whereas the latter corresponds to the void spaces directly around the now rotated tripyridyl moiety. This rotation thus allows for an increase in the void space between tripyridyl moieties of around 28%, suggesting that if the TPT-X ligands are allowed free rotation about their axes, then they can accommodate adsorbate molecules of much larger size. Furthering this, when two T4P bonds are allowed to rotate, an even larger space is created (3.19 Å, red circle in Figure 2B). This phenomenon combined with the different molecular rotator motions observed for the TPT-X ligands suggests the presence of thermally regulated mechanisms in the rotations about the T4P bonds.

Rotational Dynamics of the TPT-X Ligands in MOF-74 Pore. To more accurately model the behavior of the TPT-X ligands following their incorporation into the one-dimensional channel of MOF-74 (herein referred to as mTPT-X for TPT-X-loaded MOF), we performed multiscale DFT/XTB calculations. By modeling the TPT-X ligands in a small 12 Å section of the channel (Figure S3), we aimed to analyze how their rotational dynamics are affected by interactions within the channel environment.

Following the same scan protocol as with the DFT calculations, we observed discontinuities in the one-dimensional potential energy surfaces (Figure S13). This behavior is most likely attributed to the restrictive nature of the one-dimensional dihedral angle scans within the pore, which do not allow for sufficient rotation of the second tripyridyl moiety until a certain point is reached, causing the observed discontinuities. By performing two-dimensional scans, we can avoid these discontinuities and obtain smooth energy surfaces. Figure 3 illustrates the two-dimensional scans along the T4P dihedral angles of the four mTPT-X systems, providing a more

https://doi.org/10.1021/acs.chemmater.4c01699
Chem. Mater. 2024, 36, 8098−8106

accurate representation of their rotational dynamics within the MOF-74 channel.

In contrast to the gas-phase dihedral scans, those performed in the channel exhibit reversed behavior in which larger functional groups result in larger rotational barriers and higher overall energies. In the gas-phase, the TPT-Cl and TPT-CH_3 ligands show incredibly low energies along the entire surface, demonstrating the facile nature of the molecular rotations, while TPT-F and TPT-H result in higher energies. The effect of the pore is to raise the energy overall for all four mTPT-X systems (see Table 1). The increase in the average energy values for the mTPT-H system is the smallest, only 2.6 kJ/mol, while the other systems exhibit much larger increases of 10.9, 15.2, and 20.1 kJ mol^{-1} for TPT-F, TPT-Cl, and TPT-CH_3, respectively. These energy increases effectively indicate the formation of hindered rotator systems, where larger functional groups make rotation about the T4P bond more difficult. This suggests that once incorporated into the pore channel of MOF-74, the TPT-Cl and TPT-CH_3 ligands will require more energy to rotate about the T4P bond compared to TPT-H and TPT-F, further hinting at the possibility of temperature-controlled rotational behavior for the ligands. We would thus expect little temperature-mediated variability in the behavior of the mTPT-H and mTPT-F systems but greater variability in the mTPT-Cl and mTPT-CH_3 systems due to the differences in the energy landscapes. This behavior manifests as an increase in the pore window size with increasing temperature, which is discussed in detail below. This stark contrast between gas-phase and solid-state behavior highlights the significant impact of the MOF environment on the rotational dynamics of TPT-X ligands, indicating that gas-phase and solid-state chemistry can behave very differently in this context.

Table 1. Statistical Metrics for the Two-Dimensional Potential Energy Landscapes of the TPT-X Ligands in the Gas-Phase and in the Pore[a]

	Average	
	Gas-Phase	In-Pore
TPT-H	19.8	22.4
TPT-F	11.9	22.8
TPT-Cl	9.3	24.5
TPT-CH_3	7.7	27.8
	Standard Deviation	
	Gas-Phase	In-Pore
TPT-H	14.5	10.3
TPT-F	8.3	10.6
TPT-Cl	4.5	16.2
TPT-CH_3	6.6	16.4
	Maximum Value	
	Gas-Phase	In-Pore
TPT-H	56.5	45.8
TPT-F	35.0	49.9
TPT-Cl	19.8	73.2
TPT-CH_3	26.4	77.5

[a]Values given in kJ mol^{-1}.

Structural Effects of TPT-X Loading on MOF-74 Pore Architecture. Upon incorporating the TPT-X ligands into MOF-74, significant changes occur in the pore structure of the one-dimensional channel. To evaluate these modifications, we focus on several key properties: accessible surface area (ASA), helium pore volume (HePV), pore limiting diameter (PLD), and the largest cavity diameter (LCD). PLD values provide insights into the pore window sizes of the mTPT-X materials, while LCD and HePV characterize the volume disparities among the materials. Additionally, we consider two loading scenarios: 10% and 50%. The former corresponds to one TPT-X ligand per channel in a 1 × 1 × 5 supercell of MOF-74, while the latter represents five TPT-X ligands within the same volume. Two techniques could be utilized to create these materials including a templating approach in which the ligand is incorporating during the synthesis of the MOF[55] or a postsynthetic modification approach in which the ligand is incorporated following MOF synthesis.[56]

We conducted ten simulated annealing calculations (refer to the methods section for details) with the TPT-X ligands oriented perpendicular to the channel to determine average PLD, LCD, ASA, and HePV values for the 10% and 50% mTPT-X systems at equilibrium. We plot the latter three properties against PLD as it changes the least between the two loadings (see Figure 4). The effect of the size of the functional group can be clearly seen in the PLD values, with mTPT-H having the smallest size and therefore the largest PLD while mTPT-CH_3 and mTPT-Cl both show the smallest PLD value due to their larger size. We also see a significant change for the mTPT-CH_3 material in which the PLD value decreases 0.22 Å while the PLD values for the other materials remains constant between the two loadings.

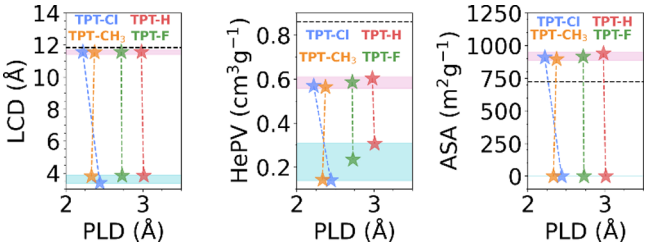

Figure 4. Changes in PLD, LCD, ASA, and HePV values for the mTPT-X systems. The shaded cyan section corresponds to 50% TPT-X loading and the shaded pink section corresponds to 10% TPT-X loading. The black dotted line represents the LCD, ASA, and HePV values of MOF-74. Color code: TPT-H (red), TPT-F (green), TPT-CH_3 (blue), TPT-Cl (yellow).

One of the most notable differences between the two loading scenarios is observed in the LCD values (left plot of Figure 4). In the case of the 50% loaded mTPT-X systems, the LCD values undergo a considerable reduction compared to the value for MOF-74 (11.95 Å). This reduction strongly implies a volumetric constraint within the system attributed to the presence of the TPT-X ligands, which occupy a substantial portion of the channel space. Conversely, when the loading is scaled down to just 10%, the LCD values closely approach that of MOF-74, indicating that much of the volume remains intact at this loading level. To quantify the extent of volume alteration, we compare the HePV values (see center plot in Figure 4) at 50% loading (less than 0.30 cm^3 g^{-1}) and 10% loading (approximately 0.60 cm^3 g^{-1}) with that of MOF-74 (0.86 cm^3 g^{-1}). These comparisons reveal that roughly two-thirds of the volume is occupied at the higher loading, while that same two-thirds is unoccupied under the lower loading.

The higher loading results in an essentially negligible value for the available surface area (right plot of Figure 4). In

https://doi.org/10.1021/acs.chemmater.4c01699
Chem. Mater. 2024, 36, 8098−8106

contrast, the lower loading materials exhibit more surface area than MOF-74 due to the additional surface area contributed by the ligands themselves, amounting to approximately 900 $m^2 g^{-1}$. Remarkably, there is about a 27% greater surface area for the mTPT-X materials compared to MOF-74, suggesting that gas storage may be more advantageous with TPT-X loading due to the presence of more favorable interactions for adsorbates.

While we position the TPT-X ligands in an idealized perpendicular orientation relative to the 1-dimensional channel of MOF-74, an alternative binding motif in which the TPT-X ligands are aligned parallel with the channel is also possible (see Figures S14–S15). The parallel binding motif results in slightly stronger binding (Table S1, calculated at the QM/XTB multiscale level of theory) to the MOF channel, which we attribute mostly to π orbital overlap between the ligand and the channel. However, we do not allow the MOF channel atoms to relax during these calculations, which may cause discrepancies in the binding energies between the perpendicular and parallel motifs.

Similarly, the stacking or aggregation of the TPT-X ligands within the MOF channel may lead to undesired results such as pore occlusion. In the gas phase, two interacting TPT-X ligands show favorable interactions in both eclipsed (AA) and staggered (AB) orientations (see Table S2). However, once incorporated into the channel, the most favorable interaction is one in which the ligands are spaced furthest apart (see Table S3). This behavior suggests that aggregation is less likely to occur, but experimental verification is necessary to confirm these findings.

Temperature-Induced Pore Dynamics in TPT-X Loaded MOF-74. Expanding now to study the dynamic behavior of the mTPT-X materials, we focus on how the PLD values change as a function of the X substituent and temperature. Here, the PLD value serves as a proxy for the size of the pore window in each material, allowing us to estimate the size of the largest adsorbate that could diffuse through the material. We do not focus on the other properties such as LCD as only small differences are observed between the low and high temperatures (Figure S17). While the simulated annealing calculations presented earlier investigated only the minimum energy structures at 0K, resulting in PLD values with very small standard deviations of less than 0.04 Å, MD simulations at nonzero temperatures reveal a distribution of PLD values (see Figure 5). These distributions offer a wealth of information on how each material changes in different temperature regimes.

The light green traces in Figure 5 depict the distribution of PLD values for the four mTPT-X materials at 100 K. Each plot exhibits distinct peaks, reminiscent of the behavior observed in Figure 2B, where rotations about the T4P bond create larger void spaces. Interestingly, the number of peaks differs among the materials, with fewer peaks observed for the mTPT-H and mTPT-F materials compared to mTPT-CH_3 and mTPT-Cl, potentially reflecting differences in the molecular rotator behavior of each TPT-X ligand. Analysis of the median PLD values (see Figure S16 and Table S4) at 100 K reveals trends consistent with the size of each substituent. Specifically, the mTPT-H material exhibits a median PLD value of 3.13 Å, while the values for mTPT-F, mTPT-CH_3, and mTPT-Cl are smaller at 2.90 Å, 2.40 Å, and 2.50 Å, respectively. This observation highlights the significant influence of the TPT-X ligand substituent on controlling the pore window size.

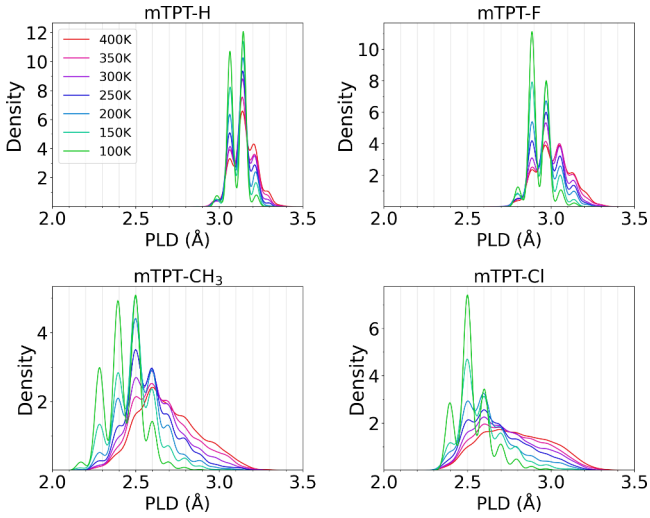

Figure 5. Kernel density estimates (KDE) of the PLD values for the 10% loading mTPT-X materials.

As the temperature of the MD simulations increases, subtle changes occur in each PLD distribution. Among the four materials, mTPT-H exhibits the smallest variation, characterized by a decrease in the height of the largest peaks at 3.06 and 3.15 Å, an increase in the height of the smallest peak at 3.23 Å, and the emergence of a new peak at 3.29 Å. These alterations result in slightly larger maximum PLD values, increasing from 3.30 Å at 100 K to 3.41 Å at 400 K, with only minor changes in the average and median PLD values (0.04 and 0.02 Å, respectively). This behavior suggests that the mTPT-H material may exhibit limited involvement in thermally regulated gating mechanisms, as the pore window size changes only marginally with temperature. The modest 3% increase in the largest PLD value indicates that the gas adsorption behavior of the mTPT-H material at 100 K would show little difference from 400 K. A similar trend is observed for the mTPT-F material, albeit with a more pronounced increase in the average and median PLD values, implying that the material spends more time with larger pore windows at higher temperatures compared to mTPT-H. Consequently, it may be slightly more inclined to participate in thermally regulated gating mechanisms, although to a limited extent. We attribute this temperature-independent behavior to the shallow energy landscapes discussed above for the 2-dimensional dihedral angle scans for mTPT-H and mTPT-F.

The PLD distributions for the mTPT-Cl and mTPT-CH_3 materials exhibit markedly different behavior compared to the mTPT-H and mTPT-F materials. Notably, the discrete peaks of the distributions almost completely disappears, resembling a "melting" of the distribution and giving rise to relatively smooth and broad distributions for mTPT-Cl and mTPT-CH_3. These distributions show much larger increases from 100 to 400 K compared to mTPT-H and mTPT-F, with both materials experiencing increases of 0.26 and 0.28 Å for the median and average PLD values, respectively. Moreover, the maximum PLD values exhibit a substantial increase of 0.42 Å (14%) and 0.33 Å (11%) for mTPT-CH_3 and mTPT-Cl, respectively, representing a significant deviation from the behavior observed in the other two materials. Although individual dihedral angles vary during the MD simulations, their impact on PLD values is influenced collectively rather than individually, with broader distributions of dihedral angles

https://doi.org/10.1021/acs.chemmater.4c01699
Chem. Mater. 2024, 36, 8098−8106

correlating to broader variations in PLD, particularly in systems with larger substituents. This observation highlights that complex interaction dynamics within the MOF pore, rather than specific angle residence times, dictate the overall pore behavior. The broadening of the PLD distributions at higher temperatures suggests that the molecular rotator behavior of the TPT-X ligands becomes more facile, enabling easier access to higher energy regions of the potential energy landscapes. Consequently, the materials spend a greater portion of time at higher PLD values, resulting in larger void spaces between the pyridyl moieties.

DISCUSSION

Our computational investigation demonstrates that integrating TPT-X (X = H, CH_3, F, Cl) ligands into the one-dimensional channels of MOF-74 creates ultramicroporous windows. The sizes of these windows are strongly influenced by both the functional group and temperature. Gas-phase DFT calculations reveal an inverse steric relationship between the substituent groups and the energy required for rotation about the T4P bond. Larger functional groups ($-CH_3$ and -Cl) exhibit smaller barriers compared to smaller groups (-H and -F). However, this behavior inverts once the ligands are incorporated into the MOF-74 channel, with larger substituents resulting in higher overall energy landscapes and much higher rotational barriers. This suggests that higher temperatures should induce much greater rotational motion in the mTPT-CH_3 and mTPT-Cl systems compared to the mTPT-H and mTPT-F systems. Consequently, these rotations should facilitate the passage of larger adsorbate molecules through the enlarged void space created postrotation at higher temperatures.

The rotational motion of the mTPT-X systems is further evidenced by changes in the PLD values with temperature. We observed that systems with smaller functional groups (mTPT-H and mTPT-F) show little dynamic behavior with temperature, exhibiting similar behavior at both 100 and 400 K. The PLD distributions show minimal variation with increasing temperature, indicating only minor differences in the size of the pore windows. In contrast, a substantial broadening of the PLD distributions was observed in the mTPT-CH_3 and mTPT-Cl systems. This is attributed to their larger functional groups and the availability of several high-energy conformations of the T4P bonds at higher temperatures. Both systems demonstrate a notable increase in the median and maximum PLD values with rising temperature. This trend suggests the potential for these systems to exhibit thermally regulated gating mechanisms, where the diffusion of gaseous adsorbates of varying sizes through the material is facilitated beyond certain activation temperatures, regulated by the functional group in the TPT-X ligand.

When compared to other ultramicroporous MOFs like ALF,[9] MUV-26,[12] and UTSA-16,[57] the mTPT-X systems showcase distinctive attributes, as depicted in Figure 6. While ultramicroporous MOFs exhibit smaller pore window sizes (PLD values) than mTPT-X, significant differences emerge in accessible surface area and helium pore volumes. At 50% loading, mTPT-X systems offer ASA values akin to ultramicroporous MOFs, albeit with minimal accessible surface area. Conversely, at 10% loading, mTPT-X systems surpass even MOF-74 in surface area due to the TPT-X ligands. These findings highlight the advantages of PSP-based systems over bespoke ultramicroporous ones. Higher loading mTPT-X

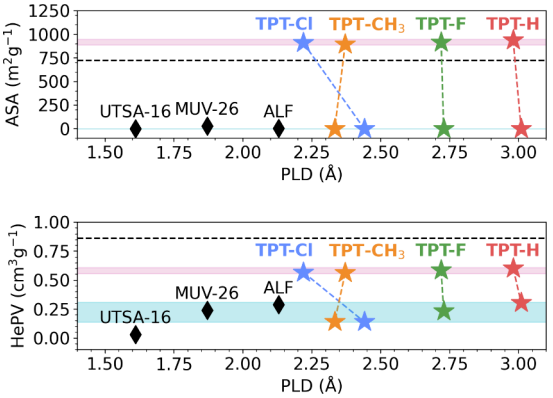

Figure 6. Changes in PLD, ASA, and HePV values for the mTPT-X systems and other ultramicroporous MOFs (black diamonds). The cyan and pink shaded sections correspond to ASA and HePV values for the 50% and 10% TPT-X loading, respectively. The black dotted line represents the ASA and HePV values of MOF-74. Color code: TPT-H (red), TPT-F (green), TPT-CH_3 (blue), TPT-Cl (yellow).

systems approach ultramicroporous MOFs in helium pore volumes which, when coupled with the ultramicroporous pore windows, suggest potential in gas separation via molecular sieving. Conversely, lower loading mTPT-X systems, with ample surface areas and helium pore volumes, show promise for gas storage,[5] leveraging their unique properties and temperature-dependent pore window size without compromising the intrinsic capacity of MOF-74. Synthesizing the mTPT-X systems may be challenging, however, and our computational endeavor assumes near-ideal behavior in terms of the loading and orientation of the TPT-X ligands with the channel of MOF-74. Nevertheless, the application of the mTPT-X systems for gas storage and separation are currently under further computational and experimental investigation in our lab.

CONCLUSION

Our computational investigation reveals that incorporating TPT-X ligands (X = H, CH_3, F, Cl) into the one-dimensional channels of MOF-74 generates ultramicroporous windows, with sizes strongly influenced by the functional group and temperature. Larger substituents ($-CH_3$ and -Cl) exhibit higher rotational barriers within the MOF-74 channel, suggesting that higher temperatures can induce greater rotational motion, facilitating the passage of larger adsorbate molecules. Notably, systems with smaller functional groups (mTPT-H and mTPT-F) show minimal temperature-dependent changes, while mTPT-CH_3 and mTPT-Cl exhibit significant broadening in pore limiting diameter (PLD) distributions at higher temperatures. This behavior points to a potential for thermally regulated gating mechanisms. Compared to other ultramicroporous MOFs, mTPT-X materials display unique advantages, such as higher accessible surface areas at lower loading and promising applications in gas storage and separation, warranting further computational and experimental exploration.

ASSOCIATED CONTENT

Data Availability Statement

Additional supporting data regarding the calculations can be found at the following repository on Zenodo: https://zenodo.org/doi/10.5281/zenodo.12760647.[58]

https://doi.org/10.1021/acs.chemmater.4c01699
Chem. Mater. 2024, 36, 8098−8106

Supporting Information

The Supporting Information is available free of charge at https://pubs.acs.org/doi/10.1021/acs.chemmater.4c01699.

Potential energy profiles along the T4P bond of the TPT-X ligands using different density functionals, along the T4P bond, and along two T4P bonds (α and β) of the TPT-X ligands, along the T4P bond of the mTPT-X ligands calculated at the DFT/XTB level of theory; 40 Å portion of the channel of MOF-74 used in multiscale calculations; 12 Å portion of the channel of MOF-74 used in the multiscale calculations; temperature and energy plots for the MD simulations; box plots and kernel density estimates for the 10% mTPT-H loaded, 10% mTPT-F loaded, 10% mTPT-CH_3, and 10% mTPT-Cl loaded MOF-74 materials as a function of simulation time; heat map depicting interatomic distances around the TPT-H ligand after zero, one, and two rotations about the T4P bonds; atomic models of the perpendicular and parallel placements of the TPT-X ligands in a 40 Å portion of the channel of MOF-74 used in multiscale calculations; formation energies between two TPT-X ligands in the channel of MOF-74 spaced *n*Mg atoms apart; box plots of PLD values; box plots and kernel density estimates of LCD values; binding energies for TPT-X ligangs; interaction energies between two TPT-X ligands in eclipsed and staggered orientations; statistical metrics for PLD values (PDF)

AUTHOR INFORMATION

Corresponding Author

Gavin A. McCarver − *National Institute of Standards and Technology, Center for Neutron Research, Gaithersburg, Maryland 20899-6102, United States;* orcid.org/0000-0002-5786-3953; Email: gavin.mccarver@nist.gov, gavin.mccarver@gmail.com

Authors

Morgan J. Kramer − *National Institute of Standards and Technology, Center for Neutron Research, Gaithersburg, Maryland 20899-6102, United States*

Taner Yildirim − *National Institute of Standards and Technology, Center for Neutron Research, Gaithersburg, Maryland 20899-6102, United States*

Wei Zhou − *National Institute of Standards and Technology, Center for Neutron Research, Gaithersburg, Maryland 20899-6102, United States;* orcid.org/0000-0002-5461-3617

Complete contact information is available at: https://pubs.acs.org/10.1021/acs.chemmater.4c01699

Notes

The authors declare no competing financial interest.

ACKNOWLEDGMENTS

G.A.M thanks NIST's Postdoctoral Program for an NRC Postdoctoral Fellowship.

REFERENCES

(1) Zhou, H.-C.; Long, J. R.; Yaghi, O. M. Introduction to Metal−Organic Frameworks. *Chem. Rev.* **2012**, *112*, 673−674.

(2) Furukawa, H.; Cordova, K. E.; O'Keeffe, M.; Yaghi, O. M. The Chemistry and Applications of Metal-Organic Frameworks. *Science* **2013**, *341*, 1230444.

(3) Zhang, X.; Chen, Z.; Liu, X.; Hanna, S. L.; Wang, X.; Taheri-Ledari, R.; Maleki, A.; Li, P.; Farha, O. K. A historical overview of the activation and porosity of metal−organic frameworks. *Chem. Soc. Rev.* **2020**, *49*, 7406−7427.

(4) Cai, G.; Yan, P.; Zhang, L.; Zhou, H.-C.; Jiang, H.-L. Metal−Organic Framework-Based Hierarchically Porous Materials: Synthesis and Applications. *Chem. Rev.* **2021**, *121*, 12278−12326.

(5) Lin, R.-B.; Xiang, S.; Zhou, W.; Chen, B. Microporous Metal-Organic Framework Materials for Gas Separation. *Chem.* **2020**, *6*, 337−363.

(6) Chan, S. P.; Zhang, Y. Ultra-Microporous and Stable MOFs with Zero-Linker Ligands for Gas Capture and Separation. *Chem. - Eur. J.* **2023**, *29*, e202301279.

(7) Wang, T.; Lin, E.; Peng, Y.-L.; Chen, Y.; Cheng, P.; Zhang, Z. Rational design and synthesis of ultramicroporous metal-organic frameworks for gas separation. *Coord. Chem. Rev.* **2020**, *423*, 213485.

(8) Ahmadi, M.; Ebrahimnia, M.; Shahbazi, M.-A.; Keçili, R.; Ghorbani-Bidkorbeh, F. Microporous metal−organic frameworks: Synthesis and applications. *Journal of Industrial and Engineering Chemistry* **2022**, *115*, 1−11.

(9) Evans, H. A.; Mullangi, D.; Deng, Z.; Wang, Y.; Peh, S. B.; Wei, F.; Wang, J.; Brown, C. M.; Zhao, D.; Canepa, P.; Cheetham, A. K. Aluminum formate, $Al(HCOO)_3$: An earth-abundant, scalable, and highly selective material for CO_2 capture. *Science Advances* **2022**, *8*, 1−11.

(10) Xie, Y.; Lin, R.; Chen, B. Old Materials for New Functions: Recent Progress on Metal Cyanide Based Porous Materials. *Advanced Science* **2022**, *9*, 2104234.

(11) Chen, B.; Eddaoudi, M.; Reineke, T. M.; Kampf, J. W.; O'Keeffe, M.; Yaghi, O. M. $Cu_2(ATC)\cdot 6H_2O$: Design of Open Metal Sites in Porous Metal−Organic Crystals (ATC: 1,3,5,7-Adamantane Tetracarboxylate). *J. Am. Chem. Soc.* **2000**, *122*, 11559−11560.

(12) Abánades Lázaro, I.; Mazarakioti, E. C.; Andres-Garcia, E.; Vieira, B. J. C.; Waerenborgh, J. C.; Vitórica-Yrezábal, I. J.; Giménez-Marqués, M.; Mínguez Espallargas, G. Ultramicroporous iron-isonicotinate MOFs combining size-exclusion kinetics and thermodynamics for efficient CO_2/N_2 gas separation. *Journal of Materials Chemistry A* **2023**, *11*, 5320−5327.

(13) Zhai, Q.-G.; Bu, X.; Zhao, X.; Li, D.-S.; Feng, P. Pore Space Partition in Metal−Organic Frameworks. *Acc. Chem. Res.* **2017**, *50*, 407−417.

(14) Wang, Y.; Jia, X.; Yang, H.; Wang, Y.; Chen, X.; Hong, A. N.; Li, J.; Bu, X.; Feng, P. A Strategy for Constructing Pore-Space-Partitioned MOFs with High Uptake Capacity for C_2 Hydrocarbons and CO_2. *Angew. Chem., Int. Ed.* **2020**, *59*, 19027−19030.

(15) Zhao, X.; Bu, X.; Nguyen, E. T.; Zhai, Q.-G.; Mao, C.; Feng, P. Multivariable Modular Design of Pore Space Partition. *J. Am. Chem. Soc.* **2016**, *138*, 15102−15105.

(16) Hong, A. N.; Yang, H.; Bu, X.; Feng, P. Pore space partition of metal-organic frameworks for gas storage and separation. *EnergyChem.* **2022**, *4*, 100080.

(17) Suh, B. L.; Lee, S.; Kim, J. Size-Matching Ligand Insertion in MOF-74 for Enhanced CO_2 Capture under Humid Conditions. *J. Phys. Chem. C* **2017**, *121*, 24444−24451.

(18) Suh, B. L.; Hyun, T.; Koh, D.-Y.; Kim, J. Rational Tuning of Ultramicropore Dimensions in MOF-74 for Size-Selective Separation of Light Hydrocarbons. *Chem. Mater.* **2021**, *33*, 7686−7692.

(19) Yang, H.; Wang, Y.; Krishna, R.; Jia, X.; Wang, Y.; Hong, A. N.; Dang, C.; Castillo, H. E.; Bu, X.; Feng, P. Pore-Space-Partition-Enabled Exceptional Ethane Uptake and Ethane-Selective Ethane−Ethylene Separation. *J. Am. Chem. Soc.* **2020**, *142*, 2222−2227.

(20) Brunet, G.; Robeyns, K.; Huynh, R. P. S.; Lin, J.-B.; Collins, S. P.; Facey, G. A.; Shimizu, G. K. H.; Woo, T. K.; Murugesu, M. Design Strategy for the Controlled Generation of Cationic Frameworks and Ensuing Anion-Exchange Capabilities. *ACS Appl. Mater. Interfaces* **2019**, *11*, 3181−3188.

(21) Yang, H.; Peng, F.; Hong, A. N.; Wang, Y.; Bu, X.; Feng, P. Ultrastable High-Connected Chromium Metal−Organic Frameworks. *J. Am. Chem. Soc.* **2021**, *143*, 14470−14474.
(22) Zhai, Q.-G.; Bu, X.; Mao, C.; Zhao, X.; Daemen, L.; Cheng, Y.; Ramirez-Cuesta, A. J.; Feng, P. An ultra-tunable platform for molecular engineering of high-performance crystalline porous materials. *Nat. Commun.* **2016**, *7*, 1−9.
(23) Forsberg, J. H.; Spaziano, V. T.; Klump, S. P.; Sanders, K. M. Lanthanide(III) ion catalyzed reaction of ammonia and nitriles: Synthesis of 2, 4, 6-trisubstituted-s-triazines. *Journal of Heterocyclic Chemistry* **1988**, *25*, 767−770.
(24) Wang, K.; Yang, L.; Wang, X.; Guo, L.; Cheng, G.; Zhang, C.; Jin, S.; Tan, B.; Cooper, A. Covalent Triazine Frameworks via a Low-Temperature Polycondensation Approach. *Angew. Chem., Int. Ed.* **2017**, *56*, 14149−14153.
(25) Biswas, S.; Batra, S. One-Step Synthesis of 2-Amino-5H-pyrimido[5, 4-b]indoles, Substituted 2-(1, 3, 5-triazin-2-yl)-1H-indoles, and 1, 3, 5-Triazines from Aldehydes. *Eur. J. Org. Chem.* **2012**, *2012*, 3492−3499.
(26) Kottas, G. S.; Clarke, L. I.; Horinek, D.; Michl, J. Artificial Molecular Rotors. *Chem. Rev.* **2005**, *105*, 1281−1376.
(27) Singhania, A.; Kalita, S.; Chettri, P.; Ghosh, S. Accounts of applied molecular rotors and rotary motors: recent advances. *Nanoscale Advances* **2023**, *5*, 3177−3208.
(28) Gonzalez-Nelson, A.; Mula, S.; Šimėnas, M.; Balčiunas, S.; Altenhof, A. R.; Vojvodin, C. S.; Canossa, S.; Banys, J.; Schurko, R. W.; Coudert, F.-X.; van der Veen, M. A. Emergence of Coupled Rotor Dynamics in Metal−Organic Frameworks via Tuned Steric Interactions. *J. Am. Chem. Soc.* **2021**, *143*, 12053−12062.
(29) Gonzalez-Nelson, A.; Coudert, F.-X.; van der Veen, M. Rotational Dynamics of Linkers in Metal−Organic Frameworks. *Nanomaterials* **2019**, *9*, 330.
(30) Gould, S. L.; Tranchemontagne, D.; Yaghi, O. M.; Garcia-Garibay, M. A. Amphidynamic Character of Crystalline MOF-5: Rotational Dynamics of Terephthalate Phenylenes in a Free-Volume, Sterically Unhindered Environment. *J. Am. Chem. Soc.* **2008**, *130*, 3246−3247.
(31) Perego, J.; Bezuidenhout, C. X.; Bracco, S.; Prando, G.; Marchiò, L.; Negroni, M.; Carretta, P.; Sozzani, P.; Comotti, A. Cascade Dynamics of Multiple Molecular Rotors in a MOF: Benchmark Mobility at a Few Kelvins and Dynamics Control by CO_2. *J. Am. Chem. Soc.* **2021**, *143*, 13082−13090.
(32) Perego, J.; Bracco, S.; Negroni, M.; Bezuidenhout, C. X.; Prando, G.; Carretta, P.; Comotti, A.; Sozzani, P. Fast motion of molecular rotors in metal−organic framework struts at very low temperatures. *Nat. Chem.* **2020**, *12*, 845−851.
(33) Gonzalez, J.; Nandini Devi, R.; Tunstall, D. P.; Cox, P. A.; Wright, P. A. Deuterium NMR studies of framework and guest mobility in the metal−organic framework compound MOF-5, $Zn_4O(O_2CC_6H_4CO_2)_3$. *Microporous Mesoporous Mater.* **2005**, *84*, 97−104.
(34) Ebadi Amooghin, A.; Sanaeepur, H.; Ghomi, M.; Luque, R.; Garcia, H.; Chen, B. Flexible−robust MOFs/HOFs for challenging gas separations. *Coord. Chem. Rev.* **2024**, *505*, 215660.
(35) Zhang, J.-P.; Zhou, H.-L.; Zhou, D.-D.; Liao, P.-Q.; Chen, X.-M. Controlling flexibility of metal−organic frameworks. *National Science Review* **2018**, *5*, 907−919.
(36) Furness, J. W.; Kaplan, A. D.; Ning, J.; Perdew, J. P.; Sun, J. Accurate and Numerically Efficient r^{2}SCAN Meta-Generalized Gradient Approximation. *J. Phys. Chem. Lett.* **2020**, *11*, 8208−8215.
(37) Grimme, S.; Hansen, A.; Ehlert, S.; Mewes, J.-M. r^{2}SCAN-3c: A "Swiss army knife" composite electronic-structure method. *J. Chem. Phys.* **2021**, *154*, 064103.
(38) Weigend, F.; Ahlrichs, R. Balanced basis sets of split valence, triple zeta valence and quadruple zeta valence quality for H to Rn: Design and assessment of accuracy. *Phys. Chem. Chem. Phys.* **2005**, *7*, 3297−3305.
(39) Ehlert, S.; Huniar, U.; Ning, J.; Furness, J. W.; Sun, J.; Kaplan, A. D.; Perdew, J. P.; Brandenburg, J. G. r^{2}SCAN-D4: Dispersion corrected meta-generalized gradient approximation for general chemical applications. *J. Chem. Phys.* **2021**, *154*, 061101.
(40) Kruse, H.; Grimme, S. A geometrical correction for the inter- and intra-molecular basis set superposition error in Hartree-Fock and density functional theory calculations for large systems. *J. Chem. Phys.* **2012**, *136*, 154101.
(41) Weigend, F. Accurate Coulomb-fitting basis sets for H to Rn. *Phys. Chem. Chem. Phys.* **2006**, *8*, 1057.
(42) Neese, F.; Wennmohs, F.; Becker, U.; Riplinger, C. The ORCA quantum chemistry program package. *J. Chem. Phys.* **2020**, *152*, 224108.
(43) Grimme, S.; Bannwarth, C.; Shushkov, P. A Robust and Accurate Tight-Binding Quantum Chemical Method for Structures, Vibrational Frequencies, and Noncovalent Interactions of Large Molecular Systems Parametrized for All spd-Block Elements (Z = 1−86). *J. Chem. Theory Comput.* **2017**, *13*, 1989−2009.
(44) Thompson, A. P.; Aktulga, H. M.; Berger, R.; Bolintineanu, D. S.; Brown, W. M.; Crozier, P. S.; in 't Veld, P. J.; Kohlmeyer, A.; Moore, S. G.; Nguyen, T. D.; Shan, R.; Stevens, M. J.; Tranchida, J.; Trott, C.; Plimpton, S. J. LAMMPS - a flexible simulation tool for particle-based materials modeling at the atomic, meso, and continuum scales. *Comput. Phys. Commun.* **2022**, *271*, 108171.
(45) Coupry, D. E.; Addicoat, M. A.; Heine, T. Extension of the Universal Force Field for Metal−Organic Frameworks. *J. Chem. Theory Comput.* **2016**, *12*, 5215−5225.
(46) Boyd, P. G.; Moosavi, S. M.; Witman, M.; Smit, B. Force-Field Prediction of Materials Properties in Metal-Organic Frameworks. *J. Phys. Chem. Lett.* **2017**, *8*, 357−363.
(47) Raza, A.; Sturluson, A.; Simon, C. M.; Fern, X. Message Passing Neural Networks for Partial Charge Assignment to Metal−Organic Frameworks. *J. Phys. Chem. C* **2020**, *124*, 19070−19082.
(48) Sarkisov, L.; Bueno-Perez, R.; Sutharson, M.; Fairen-Jimenez, D. Materials Informatics with PoreBlazer v4.0 and the CSD MOF Database. *Chem. Mater.* **2020**, *32*, 9849−9867.
(49) Newman, M. S.; Deno, N. C. Aryl Carbonium Ions in Sulfuric Acid. *J. Am. Chem. Soc.* **1951**, *73*, 3644−3650.
(50) Colter, A. K.; Schuster, I. I.; Kurland, R. J. Fluorine Magnetic Resonance Studies of Conformational Equilibria in Triphenylcarbonium Ions. *J. Am. Chem. Soc.* **1965**, *87*, 2278−2279.
(51) Schuster, I. I.; Colter, A. K.; Kurland, R. J. Magnetic resonance studies of triphenylcarbonium ions. I. Fluorine-19 nuclear magnetic resonance studies of conformational equilibria and interconversion. *J. Am. Chem. Soc.* **1968**, *90*, 4679−4687.
(52) Sundaralingam, M.; Jensen, L. H. The Structure of a Carbonium Ion. Refinement of the Crystal and Molecular Structure of sym-Triphenylcyclopropenium Perchlorate. *J. Am. Chem. Soc.* **1966**, *88*, 198−204.
(53) Ashby, M. T.; Alguindigue, S. S.; Khan, M. A. Misdirected π-donor ligands: $(\eta^5\text{-}C_5H_5)_2Zr(Cl)$ (SR) with sterically more demanding R groups have lower rotational barriers. *Inorg. Chim. Acta* **1998**, *270*, 227−237.
(54) Das, P. K.; Alguindigue, S. S.; Ashby, M. T. A DFT study of Zr-S rotational barriers of$(\eta^5\text{-}C_5H_5)_2Zr(Cl)(SR)$; the origin of an inverse steric effect. *Can. J. Chem.* **2001**, *79*, 809−816.
(55) Zhao, N.; Cai, K.; He, H. The synthesis of metal−organic frameworks with template strategies. *Dalton Transactions* **2020**, *49*, 11467−11479.
(56) Kalaj, M.; Cohen, S. M. Postsynthetic Modification: An Enabling Technology for the Advancement of Metal−Organic Frameworks. *ACS Central Science* **2020**, *6*, 1046−1057.
(57) Xiang, S.; He, Y.; Zhang, Z.; Wu, H.; Zhou, W.; Krishna, R.; Chen, B. Microporous metal-organic framework with potential for carbon dioxide capture at ambient conditions. *Nat. Commun.* **2012**, *3*, 1−9.
(58) McCarver, G.; Kramer, M.; Yildirim, T.; Zhou, W. Supporting Data for Manuscript "Unraveling Thermally Regulated Gating Mechanisms in TPT Pore-Partitioned MOF-74: A Computational Endeavor" [Data Set]. 2024, DOI: 10.5281/ZENODO.12760647.